Advances in Geo-Energy Research

Vol. 21, No. 2, p. 167-184, 2026

Original article

Dynamic evaluation of mechanical parameters and basic quality index for tunnel surrounding rock using microseismic time-lapse tomography

Hongyun Yang[1], Lunren Yang[1], Yong Li[2]*, Zhi Lin[1]*, Hucheng He[3], Ta Duong Son[4]

[1]*State Key Laboratory of Mountain Bridge and Tunnel Engineering, College of Civil Engineering, Chongqing Jiaotong University, Chongqing 400074, P. R. China*

[2]*State Key Laboratory of Coal Mine Disaster Dynamics and Control, Chongqing University, Chongqing 400044, P. R. China*

[3]*Chongqing Fengjian Expressway Co., Ltd., Chongqing 404699, P. R. China*

[4]*The National Institute of Mining-Metallurgy Science and Technology, Hanoi 11511, Vietnam*

Keywords:
Microseismic monitoring
time-lapse tomography
physical and mechanical parameters
basic quality index
dynamic analysis

Cited as:
Yang, H., Yang, L., Li, Y., Lin, Z., He, H., Son, T. D. Dynamic evaluation of mechanical parameters and basic quality index for tunnel surrounding rock using microseismic time-lapse tomography. Advances in Geo-Energy Research, 2026, 21(2): 167-184.
https://doi.org/10.46690/ager.2026.08.07

Abstract:
In deep tunneling engineering, the stability assessment and rock mass classification of the surrounding rock heavily depend on the precise acquisition of the physical and mechanical parameters and the basic quality index. However, traditional static investigation methods struggle to capture the real-time dynamic evolution of rock mass damage and the spatial heterogeneity of mechanical property degradation during excavation. To address this gap, this study uses microseismic time-lapse double-difference tomography to propose a comprehensive dynamic analysis method for evaluating the physical and mechanical parameters and the basic quality index of the tunnel surrounding rock. The results indicate that this method clearly identifies low-velocity damage zones within the surrounding rock in real time. Coupled with established relationship models correlating wave velocity with the rock properties, this approach dynamically and precisely delineates rock mass degradation zones and provides quality classifications of the surrounding rock. Influenced by excavation unloading and support installation, the surrounding rock wave velocities at different monitoring sections exhibit a distinct evolution pattern of initial steady state, unloading-induced degradation, and secondary compaction-induced recovery, accompanied by significant asymmetric spatial variations. The derived physical and mechanical parameters and the basic quality index demonstrate spatiotemporal evolution trends that are highly consistent with the wave velocity field variation. This study provides a scientific foundation and a reliable physical basis for the real-time adjustment of tunnel support designs and the early warning of instability under deep and complex geological conditions.

1. Introduction

With the extensive construction of deep tunnels worldwide, including China, increasing attention has been paid to the stability of surrounding rock around tunnels. Subjected to the combined effects of profound burial depths, elevated *in-situ* stresses, intricate geological formations, multi-field interactions within deep subsurface environments (Li et al., 2026), and construction disturbances (e.g., blasting, excavation, and support), the mechanical parameters, rock mass basic quality index (BQ), and integrity of tunnel surrounding rock evolve

Yandy Scientific Press

*Corresponding author.
E-mail address: yanghy@cqjtu.edu.cn (H. Yang); 622250780057@mails.cqjtu.edu.cn (L. Yang); yong.li@cqu.edu.cn (Y. Li); zhilin@cqjtu.edu.cn (Z. Lin); 18723216681@163.com (H. He); sontd@vimluki.vn (T. D. Son).
2207-9963 © The Author(s) 2026.
Received June 1, 2026; revised July 6, 2026; accepted July 19, 2026; available online July 22, 2026.

dynamically over time and with the construction progress (Sun et al., 2023; Zhan et al., 2024). The load-bearing capacity of the surrounding rock mass deteriorates as a consequence of fracture extension, damage accumulation and stress redistribution, making it highly susceptible to disasters such as large deformation, collapse and rockbursts (Guo et al., 2023). Therefore, achieving three-dimensional (3D), continuous and dynamic monitoring and evaluating the evolving mechanical parameters within the tunnel surrounding rock mass are essential prerequisites for ensuring construction safety and developing appropriate support and reinforcement strategies.

In traditional tunnel or rock engineering, the main methods for acquiring the mechanical characteristics of the surrounding rock mass and spatial variations thereof include laboratory compression tests on core samples, *in-situ* shear or rebound tests, and geophysical wave velocity tests (Li et al., 2024; Kong et al., 2025; Zhang et al., 2026). The primary approaches for obtaining the BQ index include core sampling and measurement, as well as *in-situ* observation (Wu and Liu, 2012; GB/T 50218-2014, 2015). Although these methods can estimate the mechanical parameters and BQ values, they have significant limitations. First, sampling and laboratory tests are restricted to a limited number of borehole locations, hence the obtained data cannot represent the spatial heterogeneity of the entire tunnel excavation zone and the surrounding rock mass. When encountering complex conditions such as joints, fissures, water saturation, and weak interlayers, generalizing from point data to a wider area involves considerable uncertainty. Second, while traditional seismic/acoustic wave velocity testing (static testing) can obtain wave velocities within a certain range, it is usually conducted prior to construction or at a specific point in time; it merely reflects the state of the medium at a "frozen moment" and lacks the capability to capture dynamic processes such as rock mass damage, fracture evolution, and stress redistribution induced by construction disturbances. Consequently, when the rock mass undergoes damage and strength degradation during construction, traditional methods often fail to detect it, or they detect it too late.

Although an advanced digital drilling process monitoring method has been developed by Li et al. (2025) to rapidly assess the mechanical properties as well as the structural integrity of the rock mass at tunnel sites, this technique remains restricted within the spatial limits of localized boreholes or excavation faces. To overcome these spatial and temporal limitations, an increasing number of researchers have recently proposed and applied microseismic monitoring as a dynamic monitoring tool. By deploying a seismic network in the tunnel or surrounding rock mass to continuously monitor microseismic events generated during construction, real-time information on microscopic processes such as fracturing and shearing within the rock mass can be obtained (Zhao et al., 2017; Ma et al., 2018).

These ongoing microseismic observations provide the data foundation for the time-lapse double-difference tomography (TomoDD) technique, which has been demonstrated as an effective dynamic seismic tomography method (Zhang and Thurber, 2003). In recent years, the implementation of time-lapse seismic imaging and TomoDD has been progressively extended to underground engineering condition monitoring, including downhole surveillance, underground mining, and tunnel surrounding rock mass monitoring (Chen et al., 2017; Qian et al., 2018; Yang et al., 2026a). Furthermore, recent studies on deformation monitoring in tunnels, as well as numerical and experimental investigations into the complex fracture behaviors of rock masses, have demonstrated the importance of the timely identification of damage zones, plastic zones, and instability trends (Sun et al., 2025; Huang et al., 2026). However, the application of four-dimensional (4D) time-lapse TomoDD during tunnel excavation remains relatively limited, as most studies primarily focus on mapping low-velocity anomaly zones and fracture propagation paths, and the inverted velocity field is usually only used as an indirect qualitative indicator of structural changes. The core focus of engineering design, support strength, and stability evaluation is often the rock mass mechanical strength, including metrics like the unconfined compressive strength and elastic modulus, whereas microseismic time-lapse imaging only directly obtains the velocity field. Therefore, to transform the time-varying velocity field into the time-varying strength field required by engineering, a mathematical or empirical relationship model between velocity and strength must be established. However, there is currently limited systematic research on establishing a quantitative conversion model between continuous 3D compressional P-wave velocity (V_p) variations and rock mass mechanical parameters as well as the BQ index.

Regarding rock and rock mass mechanics, numerous scholars have investigated and verified the correlation linking V_p to rock strength, elastic modulus, and integrity parameters (Rahman et al., 2020; Rahman and Sarkar, 2023). For instance, studies combining wave velocity tests with laboratory or *in-situ* mechanical tests (compression, shear, tension, and cohesion tests) on various rocks have shown a significant positive correlation between rock compressive strength, tensile strength, cohesion, and wave velocity. For rock types like sandstone, these relationships can be fitted using linear or power function models. This indicates that wave velocity essentially reflects the stiffness (elastic modulus) and density of the rock mass, making it highly sensitive to fracture density, damage accumulation, porosity, and the closure/propagation of cracks. Several studies have further proven that under different lithologies, water contents and fracture densities, decreases in V_p and V_s are often accompanied by a degradation of rock mass strength (Guo et al., 2023). Building upon the aforementioned theoretical and empirical evidence, it is feasible to use the 3D time-varying wave velocity field obtained from microseismic time-lapse tomography as a proxy for the rock mass strength field. As such, local reductions in V_p obtained from microseismic time-lapse tomography can serve as indicators of damage accumulation and strength degradation. In summary, this paper aims to systematically design and analyze a dynamic assessment methodology based on microseismic 3D TomoDD. This methodology is used to estimate the geomechanical parameters and BQ index of tunnel surrounding rock masses. The primary objectives include:

1) utilizing microseismic events generated during tunnel

construction as passive sources, thereby enabling continuous monitoring of the internal damage evolution and fragmentation degree in the surrounding rock mass;

2) inverting the 4D (spatial + temporal) wave velocity variation field using the time-lapse double-difference algorithm to accurately characterize the spatial evolution of damage zones and low-velocity zones in the surrounding rock mass;
3) converting the time-varying velocity field into mechanical parameter and BQ fields based on established wave velocity-parameter relationship models, and dynamically evaluating their evolution with the construction progress;
4) providing scientific support for optimizing tunnel support design, determining reinforcement timing, and issuing early warnings of rockbursts/instability.

2. Theory of microseismic TomoDD

The TomoDD method is based on the principle that closely located microseismic events recorded by the same station have comparable ray paths (Waldhauser and Ellsworth, 2000; Zhang and Thurber, 2003). The velocity structure is subsequently reconstructed by jointly inverting absolute and differential travel-time residuals between event pairs. For a microseismic event i recorded at station k, the corresponding body-wave travel time is expressed as (Zhang and Thurber, 2003):

$$T_k^i = \tau^i + \int_i^k u\mathrm{d}s \tag{1}$$

where T_k^i denotes the travel-time of the wave propagation between microseismic event i and receiver k; τ^i indicates the origin time of the event; u corresponds to the slowness vector, and ds indicates an infinitesimal integration element along the ray path.

The travel-time equation in TomoDD is nonlinear because event locations and slowness parameters, together with origin times, constitute a set of coupled unknown variables. Therefore, the nonlinear equation is linearized using a first-order Taylor expansion around a reference velocity model. Meanwhile, the velocity structure is parameterized using a three-dimensional grid-based model (Zhang and Thurber, 2003). After linearization, the above equation takes the following form:

$$r_k^i = \sum_{l=1}^{3} \frac{\partial T_k^i}{\partial x_l^i}\Delta x_l^i + \Delta\tau^i + \sum_{m=1}^{M_k}\sum_{n=1}^{N} \omega_{mn}\Delta u_n \Delta S_m \tag{2}$$

where r_k^i denotes the arrival-time residual; the total number of segments constituting the ray path connecting event i with station k is denoted by M_k; x_l^i denotes the l-th spatial coordinate of seismic event i; Δx_l^i and $\Delta\tau^i$ represent the perturbations associated with the event coordinates and origin time, respectively; ω_{mn} denotes the contribution weight of the n-th grid node to the m-th ray segment; N denotes the number of discretized velocity parameters used to describe the 3D velocity structure; Δu_n represents the slowness perturbation at the n-th grid node; and ΔS_m represents the length of the m-th ray-path segment.

Similarly, the travel-time residual from seismic j in a different time period can be written as:

$$\begin{aligned} r_k^i - r_k^j = &\sum_{l=1}^{3} \frac{\partial T_k^i}{\partial x_l^i}\Delta x_l^i + \Delta\tau^i + \int_i^k \delta u_1 \mathrm{d}s \\ &- \left(\sum_{l=1}^{3} \frac{\partial T_k^j}{\partial x_l^j}\Delta x_l^j + \Delta\tau^j + \int_j^k \delta u_2 \mathrm{d}s\right) \end{aligned} \tag{3}$$

where events i and j occur in time periods 1 and 2, respectively, with corresponding slowness parameters δu_1 and δu_2; the differential residual obtained at station k from the event pair consisting of i and j is denoted by $r_k^i - r_k^j$; T_k^j denotes the theoretical arrival time from event j to station k; Δx_l^j and $\Delta\tau^j$ represent the perturbations of the location and origin time of event j, respectively; the terms $\int_i^k \delta u_1 \mathrm{d}s$ and $\int_j^k \delta u_2\, ds$ describe the travel-time perturbations resulting from slowness variations along the propagation paths during the two respective monitoring stages.

When two microseismic events are located close to each other, their ray paths reaching the same station are approximately similar, resulting in nearly identical travel-time perturbations caused by velocity variations along these paths. Therefore, the travel-time effects induced by velocity perturbations for the two events are assumed to be approximately equivalent. Eq. (3) can be further simplified to:

$$\mathrm{d}r_k^{ij} = r_k^i - r_k^j = \frac{\partial T_k^i}{\partial p}\Delta p^i + \Delta\tau^i - \left(\frac{\partial T_k^j}{\partial p}\Delta p^j + \Delta\tau^j\right) \tag{4}$$

where the double-difference travel-time residual between events i and j observed at station k is denoted by $\mathrm{d}r_k^{ij}$; p denotes the model parameter vector; $\partial T_k^i/\partial p$ represents the sensitivity of travel time to the model parameters; Δp^i and Δp^j represent the corresponding model parameter corrections for the two seismic events; the perturbations of the origin times for events i and j are denoted by $\Delta\tau^i$ and $\Delta\tau^j$, respectively. After the double-difference operation, the influence of the velocity structure is largely suppressed, and the remaining residual is mainly attributed to the discrepancies in event locations and origin times. The corresponding double-difference residual is obtained by comparing the observed differential travel time with the calculated value predicted by the theoretical model for the event pair:

$$dr_k^{ij} = r_k^i - r_k^j = \left(T_k^i - T_k^j\right)^{obs} - \left(T_k^i - T_k^j\right)^{cal} \tag{5}$$

where superscripts "obs" and "cal" are used to distinguish observed quantities from calculated ones.

Iteratively solving Eqs. (4) and (5) using the least squares method yields highly accurate source locations independent of velocity structure perturbations, providing the theoretical foundation for double-difference-based event relocation. However, if the distance between seismic events becomes larger than the characteristic length of velocity heterogeneity, the assumption of similar ray paths becomes invalid, leading to reduced relocation reliability. Furthermore, the conventional double-difference relocation approach does not explicitly account for travel-time variations associated with velocity changes along the ray paths. To overcome this issue, double-difference tomography directly utilizes Eq. (3) to couple event locations

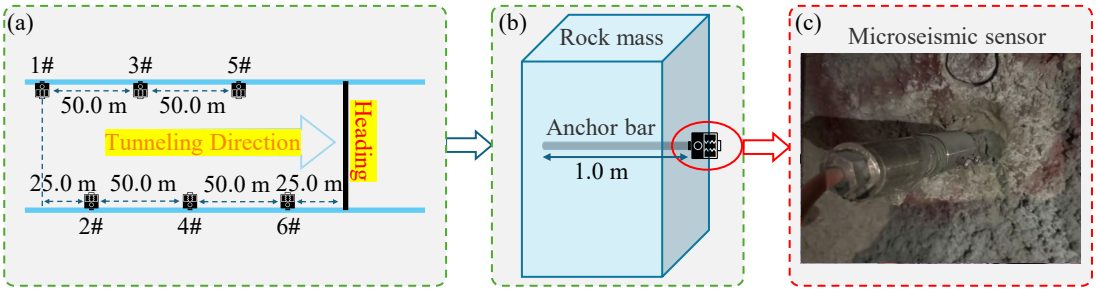


Fig. 1. Layout of the microseismic sensors: (a) Layout scheme of the sensors along both sidewalls, (b) schematic diagram of sensor installation at the ends of rock bolts and (c) actual field installation photo.

and velocity structure. By simultaneously solving Eqs. (3) and (5), both the absolute and the relative travel times are utilized, enabling synchronous velocity imaging and accurate source relocation.

The coupled inversion combines absolute and differential travel-time information, with the former constraining the background velocity field and the latter improving local structural resolution. This mutual constraint reduces errors, yielding more accurate velocity structures and event locations compared to standard methods (Waldhauser and Ellsworth, 2000).

Building upon this robust theoretical foundation, which has been extensively applied in regional tectonic, underground mining, and reservoir monitoring studies (Chen et al., 2017; Qian et al., 2018), the TomoDD framework was further extended to applications involving challenging tunnel engineering conditions by Yang et al. (2026a, 2026b). Rather than altering the classical algorithm, the present study advances this engineering application through three main contributions:

1) transitioning from qualitative velocity anomaly identification to the quantitative evaluation of dynamic rock mass properties and BQ indicators (e.g., BQ index) driven by the inverted V_p field;
2) shifting from static geophysical imaging to 4D time-lapse dynamic tracking, which continuously updates the 3D velocity model synchronously with excavation to capture progressive unloading damage;
3) enhancing the spatial resolution from macroscopic regional applications to high-precision surrounding rock mass characterization.

3. Dynamic evolution analysis of wave velocity

3.1 Engineering background

Geographically, the experimental section of the Xiaoying Tunnel is located in Wushan County, Chongqing Municipality, with the tunnel dimensions measuring 5.0 m in height and 10.25 m in span. The experimental section is located in the left tunnel, extending from chainage K42+671 to K42+743, with a total length of 72 m and a burial depth ranging from 730.950 to 802.994 m, and its elevation is between 890 and 900 m.

Geologically, the experimental tunnel section is located in Member 2 within the Lower Triassic Daye Formation. The lithology is predominantly light gray limestone intercalated with thin-layered argillaceous limestone and shale bands, with a strike of 335° and a dip of 15°. The surrounding rock mass is classified as relatively hard rock, with a comparatively intact to intact structure.

3.2 Wave velocity monitoring scheme

To enable high-precision characterization of the surrounding rock behavior during tunnel excavation, microseismic sensors were deployed in an alternating layout along both tunnel sidewalls, with a spacing of 25 m between adjacent sensors, as shown in Fig. 1(a). This alternating layout along both sidewalls constructs a reliable 3D spatial network, effectively increasing the cross-coverage rate of seismic rays, eliminating location blind zones caused by linear arrays, and providing fundamental travel-time data constraints for the 3D double-difference tomography.

The sensors were installed at the rock bolt ends, as shown in Figs. 1(b) and 1(c). The rock bolts were 1.0 m long and fully grouted. This installation method achieves excellent rigid coupling between the sensors and the bolts. Compared to traditional in-hole installation methods, this configuration enables the acquisition of fracture-related microseismic signals characterized by stronger amplitudes, improved signal quality, more distinct waveform features, and extended effective durations. Simultaneously, further enhancements are achieved in spectral stability, low-frequency response, high-frequency noise suppression, and signal dynamic range. Consequently, the overall SNR and anti-interference ability are substantially improved, enhancing the suitability of this setup for microseismic signal analysis and providing a reliable guarantee for the real-time dynamic monitoring of the evolution of hidden damage zones (Yang et al., 2026a, 2026b).

Two monitoring sections, K42+671 (the tunnel face on 24th June) and K42+685, were established within the tunnel, with four wave velocity analysis points set up on each, as shown in Fig. 2. As shown in the figure, the spacing between the two monitoring sections is 14.0 m. The wave velocity analysis points 1 and 3 are located 5 m above the tunnel roof and 5 m below the tunnel floor, respectively, while points 2 and 4 are located 5 m from the corresponding sidewalls of the tunnel.

3.3 Analysis of monitoring results

All valid microseismic events recorded during the entire monitoring period were statistically analyzed, as shown in

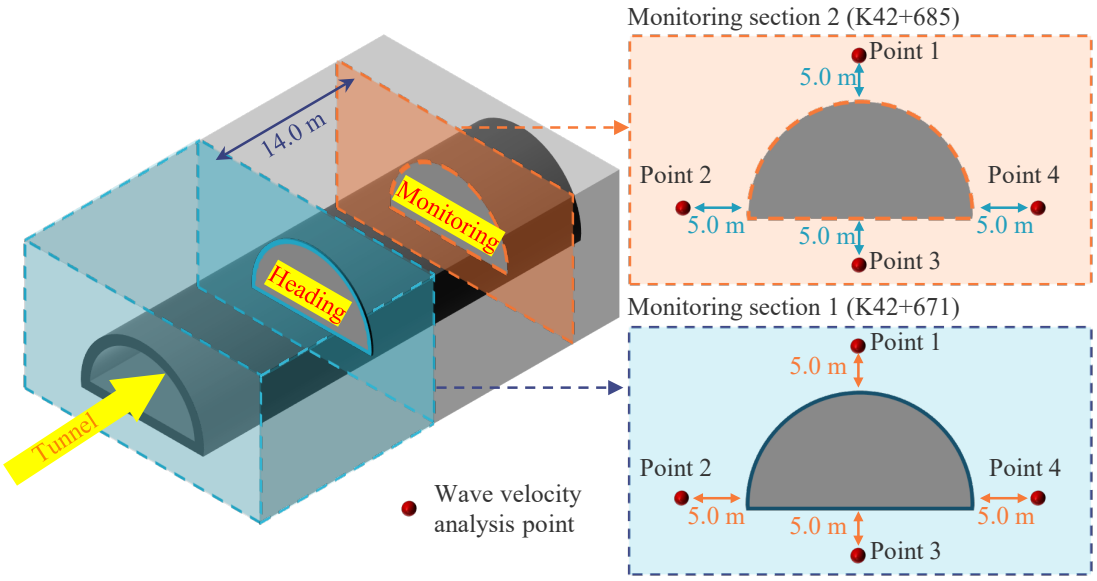


Fig. 2. Sensor layout scheme and monitoring sections.

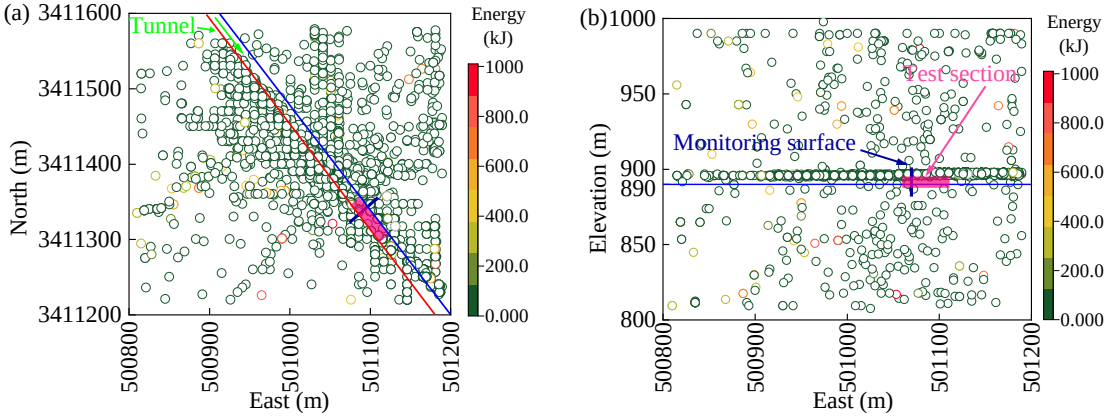


Fig. 3. 3D spatial scatter distribution map of localized microseismic events throughout the entire monitoring period: (a) Horizontal and (b) vertical direction.

Fig. 3. The figure displays the distribution characteristics of these microseismic events along both the horizontal and vertical directions of the tunnel. The microseismic events exhibit a distinctly non-uniform spatial distribution, primarily concentrated in the excavation-influenced zone and locally disturbed areas of the surrounding rock mass, providing a solid data foundation for subsequent (TomoDD).

On the basis of the identified excavation-disturbed zones and localized damage areas revealed by the microseismic event distribution, the temporal evolution of V_p in the surrounding rock mass at two representative monitoring sections (K42+671 and K42+685) was further analyzed over a 21-day period from 24th June to 14th July, as shown in Fig. 4.

For the monitoring section K42+671, the temporal evolution characteristics of V_p are presented in Fig. 4(a). During the initial monitoring stage, the wave velocity at each analysis point remains stable around 6.7 km/s, indicating that the rock mass maintains a relatively high degree of integrity under the original *in-situ* stress state. Starting from 30th June, affected by the disturbance of excavation unloading, the wave velocity exhibits a step-like decrease with significant asymmetry. The wave velocity at analysis point 2 on the left sidewall drops to 6.463 km/s on 3rd July, experiencing the maximum decrease, indicating highly developed micro-fractures. After 5th July, the wave velocity rapidly recovers and then stabilizes at a high-level range of 7.1 km/s after 7th July, entering the secondary compaction stage.

To further reveal the differential evolution of damage in the surrounding rock induced by excavation disturbance, the temporal variation in wave velocity at the representative monitoring section K42+685 was analyzed. Fig. 4(b) illustrates the dynamic response pattern of wave velocity at this section. The excavation damage effect is particularly concentrated and severe, with a sudden drop in wave velocity between 30th June and 1st July. The wave velocity at analysis point 2 on the left sidewall reaches a minimum value of 6.335 km/s, indicating

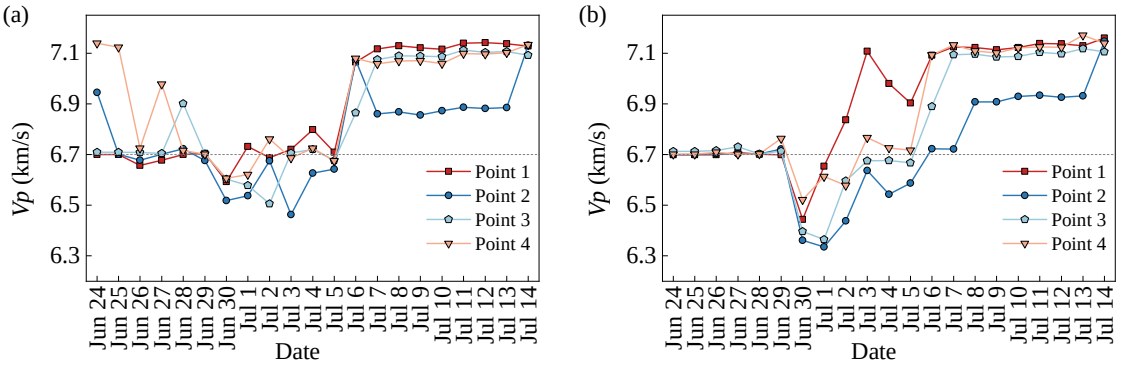


Fig. 4. Monitoring results of wave velocity in the tunnel surrounding rock mass: Wave velocity variations at four analysis points on (a) section K42+671 and (b) section K42+685.

severe local damage and degradation. The wave velocity at analysis point 1 at the vault rebounds at an extremely fast rate, exceeding 7.1 km/s first on 3rd July. This reflects the strong hoop compressive stress existing in the vault area, which, together with the support structure, drives the rapid closure of structural planes and micro-fractures.

To comprehensively evaluate the spatial heterogeneity and temporal evolution characteristics of excavation-induced damage, the wave velocity variations at the two monitoring sections were further compared. Figs. 4(a) and 4(b) collectively demonstrate the spatial anisotropy and periodicity of the spatiotemporal evolution within the surrounding rock mass. Spatially, the significant degradation of wave velocity at the four analysis points confirms that the excavation damage zone has a large-scale spatial extent. Damage development within the surrounding rock mass shows a pronounced asymmetric pattern, with the left sidewall consistently acting as the vulnerable core area, experiencing the largest drop and the slowest recovery in wave velocity. The recovery rates and stabilized values of the vault and the right sidewall are significantly higher. Temporally, the two sections, spaced 14.0 m apart, both undergo a complete life cycle of "initial steady state, unloading damage, and secondary compaction hardening", showing a high degree of spatiotemporal consistency.

The radial stress transfer induced by excavation unloading in deep tunnels promotes the overall mechanical densification of the deep-seated media in the surrounding rock mass, causing the absolute wave velocities during the stable period to exceed the initial baseline values. The spatially asymmetric fracture mode is directly related to the biased distribution of the regional initial geo-stress or the cutting by specific structural planes, making the left side more prone to crack initiation.

The variations in the rock mass wave velocity within a range of 50 m on both sides of the tunnel at an elevation of 890 m (6.050 m below the tunnel floor) and the roof elevation of 900 m (2.250 m above the tunnel roof) on 23rd June and 24th June were plotted in Fig. 5. For the same monitoring period, the wave velocities of rock mass at different elevations exhibit significant differences. Specifically, the wave velocity distribution pattern at the 900-m roof is more complex than that at the 890-m floor, with more and deeper low-velocity anomalous zones appearing, as indicated by the red or orange concave areas in the figure. At the same elevation, the rock mass wave velocity changes drastically across different time periods, showing obvious time-varying characteristics of the V_p. It can be observed that within just one day, the wave velocity field undergoes dramatic changes. Especially in the longitudinal section of 800-900 m, the morphology, extent and extreme values of the low-velocity anomalies exhibit marked evolution.

In summary, the wave velocity possesses significant spatial and temporal variation characteristics. By utilizing microseismic TomoDD, the V_p can be dynamically acquired within the surrounding rock mass, enabling real-time monitoring of the wave velocity variations in the tunnel surrounding rock mass.

3.4 Field validation and mechanical interpretation

3.4.1 Validation using field geotechnical monitoring data

The practical reliability of the inverted wave velocity field was evaluated by analyzing and comparing *in-situ* conventional geotechnical deformation monitoring data (crown settlement, sidewall displacements, and peripheral convergence) at section K42+685 with the inverted V_p time series (Fig. 4). As shown in Fig. 6, macroscopic deformation trends exhibit strong temporal consistency and stage-by-stage correspondence with microscopic V_p deterioration across three distinct phases:

Rapid deformation and V_p degradation phase (29th June-2nd July): Excavation unloading induces rapid growth in crown settlement and peripheral convergence. Quantitatively, V_p at section K42+685 drops from the initial 6.70 to 6.30 km/s, representing a maximum wave velocity degradation rate of 5.97%. This degree of velocity attenuation quantitatively corresponds to an initial deformation rate peaking at 1.5 mm/d and a maximum cumulative displacement of $3.8 \sim 4.8$ mm, reflecting micro-crack propagation and structural integrity degradation under excavation disturbance.

Deformation deceleration and V_p recovery phase (3rd July-7th July): The deformation growth rate gradually slows, while V_p rapidly recovers following brief fluctuations. Primary sup-

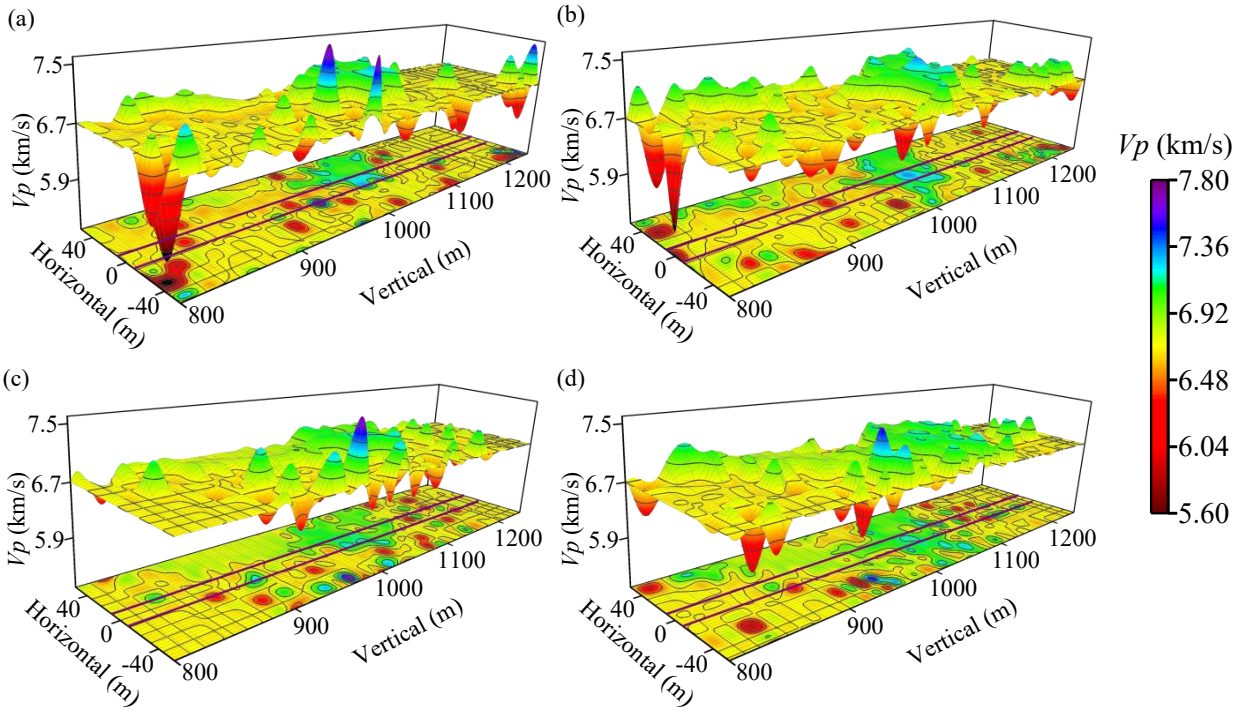


Fig. 5. Rock mass wave velocity within a range of 50 m on both sides of the tunnel: (a) 890-m floor on 23rd June, (b) 900-m roof on 23rd June, (c) 890-m floor on 24th June and (d) 900-m roof on 24th June.

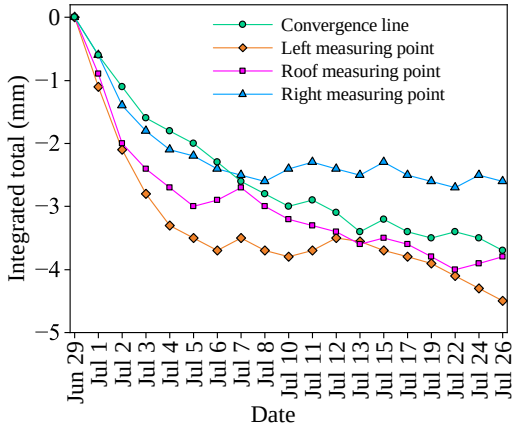


Fig. 6. Measured conventional geotechnical deformation time series at section K42+685.

port installation: V_p at certain analysis points rebound to ~7.1 km/s around 7th July, indicating fracture closure and initial rock mass compaction.

Stable deformation and V_p stabilization phase (After 7th July): As structures take full effect, the confinement support is installed and the confinement recovered, the displacement growth rate approaches 0 mm/d. Correspondingly, V_p values rebound and stabilize at 7.10-7.20 km/s (representing a maximum compaction-induced increase of 7.46% over the initial baseline) without further attenuation, demonstrating that the internal damage evolution is effectively controlled.

This explicit numerical mapping between the velocity variation ratio ($\Delta V_p/V_{p0} = 5.97\%$) and cumulative displacement magnitude ($\Delta S = 4.8$ mm) establishes a clear multi-scale correlation between macroscopic geotechnical deformation and microscopic velocity evolution, providing solid quantitative field evidence for the reliability of microseismic V_p inversion.

3.4.2 Asymmetric damage evolution mechanism

To elucidate the mechanical origin of the spatial asymmetry observed in V_p evolution, high-precision digital image processing of cross-section K42+689 was conducted, revealing a gentle left-dipping apparent dip of 4.1° (Fig. 7(b)). This structural orientation forms an anti-dip intersection on the left wall and a dip intersection at its right counterpart (Fig. 7(c)).

On the left (anti-dip) side, excavation releases radial constraint (σ_r) and concentrates tangential stress (σ_θ), generating a sharp radial stress gradient (Figs. 7(c) and 7(d)). Under this unfavourable geometry, stress deflection and bending moments shift the stress state from pure compression to flexural tension. As flexural buckling intensifies and bending tensile stresses exceed matrix tensile strength, interlayer opening and cross-bedding tensile fractures develop. This matrix fracturing and dilation drive microseismic activity deep into the rock mass, causing continuous V_p reduction.

Conversely, the right (dip) side exhibits a dip-cutting relationship (Figs. 7(c) and 7(e)). In the superficial layer, rock masses undergo shear slipping along the bedding planes. With increasing depth, the radial constraint (σ_r) recovers, transitioning the stress state into triaxial compression. Under high deep confinement, shear dilation triggers passive resistance from the surrounding rock mass, significantly increasing normal stress (σ_{n2}) acting on the bedding planes. According to the Mohr-Coulomb criterion ($\tau_f = c + \sigma_{n2}\tan\varphi \gg \tau$), elevated normal stress substantially enhances shear strength (τ_f) well

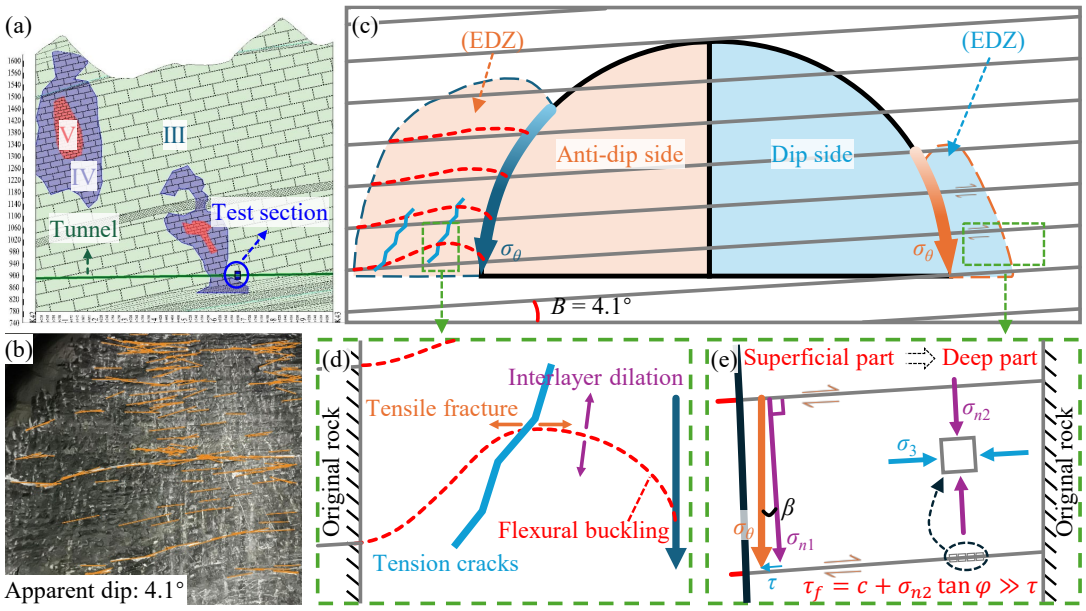


Fig. 7. Asymmetric damage evolution mechanism of layered surrounding rock with a 4.1° apparent dip: (a) Geological profile near the test section, (b) structural plane distribution at section K42+689, (c) macroscopic mechanical model of asymmetric failure and (d)-(e) micromechanical failure mechanisms on the anti-dip and dip sides.

beyond the shear stress component (τ). This creates a robust frictional interlocking effect that seals deep damage pathways and suppresses fracture propagation, thereby maintaining high and stable V_p values within the deeper right side of the surrounding rock.

3.4.3 Comparison with TSP advanced geological forecasting

To highlight the unique value of dynamic microseismic imaging over static pre-excavation surveys, a horizontal comparative analysis was conducted between the inverted V_p results (Fig. 4) and the tunnel seismic prediction (TSP) data (Fig. 8) acquired during construction. The TSP method utilizes active seismic reflections to identify macroscopic lithological boundaries and major adverse geological structures located ahead of the tunnel face.

For the monitoring range (K42+492 to K42+692), the TSP forecasting report in Fig. 8 shows relatively gentle V_p and V_s variations from section K42+671 to K42+692, with an *in-situ* baseline V_p of 5.74 km/s. In comparison, the inverted microseismic V_p during the excavation damage process ranges between 6.35 and 7.20 km/s (with an initial baseline of 6.70 km/s and a damaged-state minimum of 6.30 km/s). Quantitatively, the damaged-state velocity (6.30 km/s) exhibits a relative deviation of only 9.8% from the TSP baseline, while the initial baseline deviation is 16.7%, maintaining the overall relative error within 9.8%-16.7%, with the damaged-state deviation satisfying the $< 15\%$ quantitative accuracy limit in engineering geophysics. This minor discrepancy is physically attributed to wave dispersion across observation frequencies and tangential stress concentration near the wall, while the subsequent V_p rebound to 7.20 km/s reflects rock mass secondary compaction induced by the combined effects of stress redistribution and lining support, rather than a background velocity measurement artifact.

This result highlights the differences in observation scale and information dimensions: TSP provides a pre-construction macroscopic geological baseline, whereas microseismic tomography reveals high-resolution, post-disturbance local damage evolution. Consequently, dynamic microseismic imaging serves as a vital complement to traditional advanced geological forecasting, extending the monitoring paradigm from "macroscopic geological prediction" to "dynamic damage monitoring".

4. Analysis of dynamic rock mass mechanical parameters

During tunnel excavation, the physico-mechanical state of the surrounding rock undergoes significant spatiotemporal evolution. Microseismic TomoDD enables inversion of the time-dependent V_p field within the surrounding rock mass. This study, based on existing empirical models relating V_p to rock mass mechanical parameters, characterizes the dynamic evolution of the surrounding rock.

4.1 Relationship of V_p and rock mass mechanical parameters

4.1.1 Correlation with V_p

Within the realm of rock engineering, the Hoek-Brown (H-B) failure criterion remains one of the most widely adopted methodologies for evaluating the mechanical properties of rock masses (Hoek et al., 2002; Hoek and Brown, 2019). This criterion leverages the geological strength index (GSI) to provide a quantitative assessment of rock mass strength, inherently factoring in internal structural traits and discontinuity states.

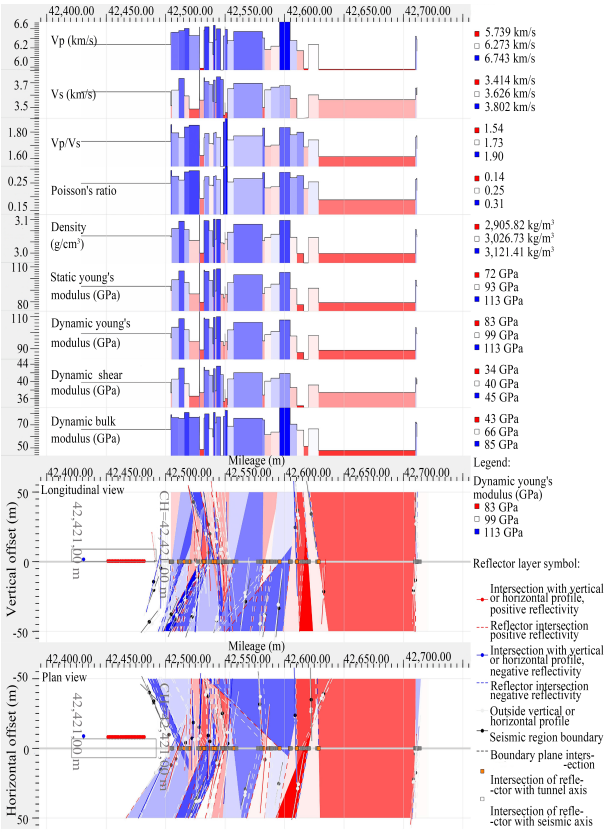


Fig. 8. TSP 203 advanced geological forecasting report results covering chainage K42+492 to K42+692.

Furthermore, the influence of excavation unloading and subsequent structural disturbances on mechanical behavior is accounted for via the disturbance factor D (Cui et al., 2017; Feng et al., 2018; Xia et al., 2022a, 2022b, 2024). The generalized form of the H-B strength criterion is expressed as (Hoek et al., 2002):

$$\sigma_1 = \sigma_3 + \sigma_c \left(m_b \frac{\sigma_3}{\sigma_c} + s \right)^a \tag{6}$$

where σ_c stands for the intact rock's uniaxial compressive strength obtained through laboratory testing, whereas σ_1 and σ_3 designate the major and minor principal stresses at the point of failure, respectively. The terms m_b, s and a represent empirical constants specific to the evaluated rock mass and are calculated using the formulas below (Hoek et al., 2002):

$$m_b = m_i \exp\left(\frac{\mathrm{GSI}-100}{28-14D}\right) \tag{7}$$

$$s = \exp\left(\frac{\mathrm{GSI}-100}{9-3D}\right) \tag{8}$$

$$a = \frac{1}{2} + \frac{1}{6}\left[\exp\left(-\frac{\mathrm{GSI}}{15}\right) - \exp\left(-\frac{20}{3}\right)\right] \tag{9}$$

where m_i refers to the material constant of intact rock, derived from empirical classification tables introduced by Hoek and Brown (1997) as well as Marinos and Hoek (2001).

Prior research has established quantitative links connecting the compressional wave velocity V_p of the rock mass with both GSI and D (Somodi et al., 2018; Xia et al., 2022a):

$$\mathrm{GSI} = 15V_p - 2.5 \tag{10}$$

$$D = 2\left\{1 - \exp\left[\frac{15\left(V_{p,d} - V_{p,ud}\right)}{36}\right]\right\} \tag{11}$$

In the equations above, $V_{p,ud}$ and $V_{p,d}$ indicate the P-wave velocities measured within undisturbed and disturbed rock masses, respectively.

Because the variables D and GSI are integral to the computation of the rock mass material parameters (as seen in Eq. (9)), a definitive correlation exists between V_p and these characterizing metrics.

Uniaxial compressive strength of rock mass:

$$\sigma_{cm} = \sigma_c s^a \tag{12}$$

Uniaxial tensile strength of rock mass:

$$\sigma_{tm} = \frac{1}{2}\sigma_c\left[m_b - \left(m_b^2 + 4s\right)^a\right] \tag{13}$$

Deformation modulus of rock mass:

$$E_m = \begin{cases} \exp\left[\dfrac{15\left(V_{p,d} - V_{p,ud}\right)}{36}\right]\sqrt{\dfrac{\sigma_c}{100}}\,10^{(15V_{p,ud}-12.5)/40}, \\ \sigma_c \le 100\,\mathrm{MPa} \\ \exp\left[\dfrac{15\left(V_{p,d} - V_{p,ud}\right)}{36}\right]10^{(15V_{p,ud}-12.5)/40}, \\ \sigma_c > 100\,\mathrm{MPa} \end{cases} \tag{14}$$

When operating within the stress range of $\sigma_m < \sigma_3 < \sigma_{3\max}$ (where $\sigma_{3\max}$ denotes the maximum normal stress), the nonlinear curve of the H-B failure criterion aligns closely with the Mohr-Coulomb (M-C) failure criterion curve. By applying a linear fit between the H-B and M-C criteria, one can determine the rock mass shear strength parameters, namely cohesion (c) and internal friction angle (φ), using the following equations (Hoek et al., 2002):

$$c = \frac{\sigma_c\left[(1+2a)s + (1-a)m_b\sigma'_{3n}\right]\left(s + m_b\sigma'_{3n}\right)^{a-1}}{(1+a)(2+a)\sqrt{1 + \dfrac{6am_b\left(s+m_b\sigma'_{3n}\right)^{a-1}}{(1+a)(2+a)}}} \tag{15}$$

$$\varphi = \sin^{-1}\left[\frac{6am_b\left(s+m_b\sigma'_{3n}\right)^{a-1}}{2(1+a)(2+a) + 6am_b\left(s+m_b\sigma'_{3n}\right)^{a-1}}\right] \tag{16}$$

where σ'_{3n} denotes the normal stress, and $\sigma'_{3n} = \sigma_{3\max}/\sigma_c$.

As established by Eqs. (10) and (11), the indices GSI and D are mathematically dependent on V_p and they in turn govern the foundational material constants m_b, s and a (as shown in Eqs. (7)-(9)). Ultimately, because these constants dictate all mechanical properties derived from the H-B failure criterion, including deformation modulus, uniaxial strengths, cohesion, and internal friction angle, an indirect yet robust linkage is forged. Therefore, any mechanical parameters deduced through this framework exhibit a profound correlation with V_p.

4.1.2 Density and dynamic elastic parameters

Drawing upon the elastic wave theory, the mathematical relationships connecting the mechanical parameters (specifically ρ, E_d, G_d, and μ_d) to the wave velocity are outlined as follows (Gardner et al., 1974; Ben Ghawar et al., 2021):

Rock mass density:

$$\rho = aV_p^b \tag{17}$$

where a and b represent empirical parameters, typically taking values of $a = 0.31$ and $b = 0.25$.

Calculation formula for the dynamic elastic modulus:

$$E_d = V_p^2\rho\frac{(1+\mu_d)(1-2\mu_d)}{1-\mu_d} = \rho V_s^2\frac{3V_p^2-4V_s^2}{V_p^2-V_s^2} \tag{18}$$

Calculation formula for the dynamic shear modulus:

$$G_d = \frac{E_d}{2(1+\mu_d)} = \rho V_p^2\frac{1-2\mu_d}{2(1-\mu_d)} = \rho V_s^2 \tag{19}$$

Calculation formula for the dynamic Poisson's ratio:

$$\mu_d = \frac{V_p^2-2V_s^2}{2\left(V_p^2-V_s^2\right)} \tag{20}$$

Determining the dynamic parameters for the surrounding rock in Eqs. (17)-(20) primarily relies on both V_p and V_s. However, due to the low S-wave energy and high picking uncertainties typically encountered in field microseismic data, a constant S-wave velocity of $V_s = 3.7$ km/s is adopted across Eqs. (18)-(20) to avoid subjective errors. Under this constant V_s assumption, the variables in Eqs. (17)-(20) become explicitly dependent on the V_p term. This demonstrates that the dynamic mechanical properties of the rock mass, including density, Poisson's ratio, elastic modulus, and shear modulus, are primarily governed by V_p, providing equivalent dynamic parameters that reliably capture the relative spatial evolution trends of the surrounding rock mass.

In summary, the mechanical parameters of rock mass obtained from either the H-B failure criterion or the elastic wave theory exhibit significant relationships with V_p. Therefore, the latter can be used as a proxy index to reflect the rock mass mechanical parameters, serving as a key characterization parameter linking the physical state and mechanical response of the rock mass.

4.2 3D mapping of mechanical parameters

4.2.1 Density and V_p

After obtaining the time-dependent V_p field for the surrounding rock, the corresponding mechanical parameters can be dynamically inverted using established velocity-parameter conversion models. By comparing and analyzing the inversion results at different times, the temporal evolution of mechanical indices in the surrounding rock can be characterized, including density, dynamic Poisson's ratio, compressive strength, and dynamic elastic modulus, with respect to the construction progress. The time-varying mechanical parameter fields obtained in this study are primarily used to characterize the relative variation trends of the mechanical properties of the surrounding rock mass, and the results can provide a basis for identifying potential damage zones, low-velocity anomalies, and areas of rock mass quality degradation.

The calculation of rock mass density follows Eq. (17), where $a = 0.31$ and $b = 0.25$ were adopted. The wave velocity and density of the rock mass within a 30 m range of the K42+685 monitoring section on 24th June are shown in Fig. 9.

To validate the density distribution derived from the wave velocity-density relationship model and investigate the evolution of surrounding rock mechanical parameters at the early excavation stage, a comparative analysis of the wave velocity field and the density field at the K42+685 monitoring section was conducted. From the results presented in Figs. 9(a) and 9(b), the wave velocity of the rock mass fluctuates around 6.7 km/s, with the mean value of wave velocity being 6.708 km/s. The overall wave velocity is relatively stable and no obvious low-velocity zones are formed. Specifically, small low-velocity regions can be identified at the upper-middle and lower-left positions of the 890-m floor, while no such anomalies appear in the 900-m roof. The reason is that, by 24th June, the tunnel face had not yet reached the monitoring section and was located 14 m behind the monitoring section. The relatively long distance between the monitoring section and the tunnel face indicates that excavation had a limited influence on the surrounding rock at the monitoring section.

Corresponding to Figs. 9(a) and 9(b), the rock mass density maps in Figs. 9(c) and 9(d) show that density fluctuates roughly around 2.80 g/cm^3, with its average value being 2.805 g/cm^3, indicating a small density variation. On 24th June, prior to the arrival of the tunnel face, both the wave velocity and density fields at section K42+685 were highly stable. Since the rock mass density is calculated from V_p according to Eq. (17), the density distribution exhibits a spatial pattern consistent with the baseline velocity field before excavation.

4.2.2 Dynamic Poisson's ratio and V_p

Eq. (20) was employed to calculate the Poisson's ratio, with V_s taken as 3.7 km/s. The wave velocity and Poisson's ratio of the rock mass within a 30 m range of the K42+685 monitoring section on 30th June are shown in Fig. 10.

To investigate the variation characteristics of the mechanical properties of surrounding rock after the tunnel face approached the monitoring section, the spatial distributions of V_p and Poisson's ratio at the K42+685 monitoring section were analyzed. The wave velocity distributions on 30th June are presented in Figs. 10(a) and 10(b). The V_p of the rock mass is mostly below 6.7 km/s, characterized by a mean V_p of 6.494 km/s. The rock mass V_p is generally low, specifically manifested as low wave velocities within the 890 m and 900 m tunnel areas and the 15 m range on both sides. The wave velocities of the surrounding rock mass are slightly higher than those inside the tunnel, forming obvious low-velocity zones. On the right side of the 900-m roof, there are a few areas where the wave velocity is higher than that of the 890-m floor. The reason is that by 30th June, the tunnel face had advanced to 3 m past the monitoring cross-section. Only a short distance separated the tunnel face from the monitoring cross-section,

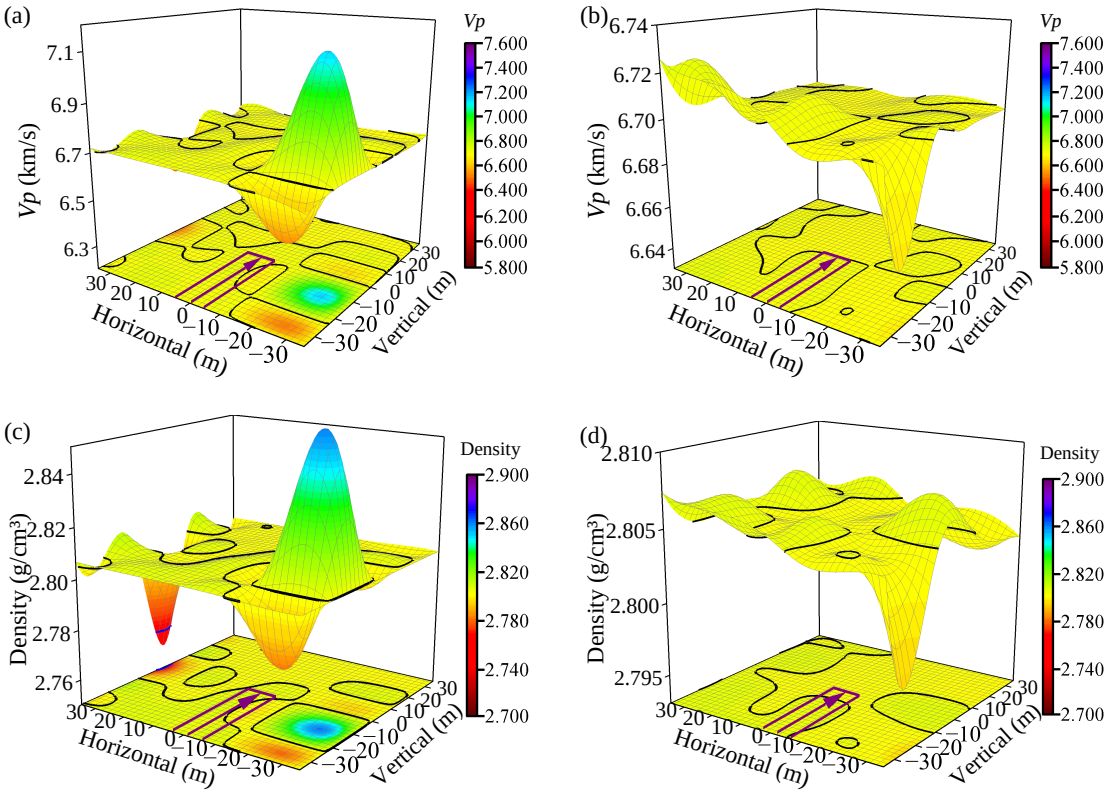


Fig. 9. Wave velocity and density of the rock mass at the K42+685 monitoring section on 24th June: (a) 890-m floor (wave velocity), (b) 900-m roof (wave velocity), (c) 890-m floor (density) and (d) 900-m roof (density).

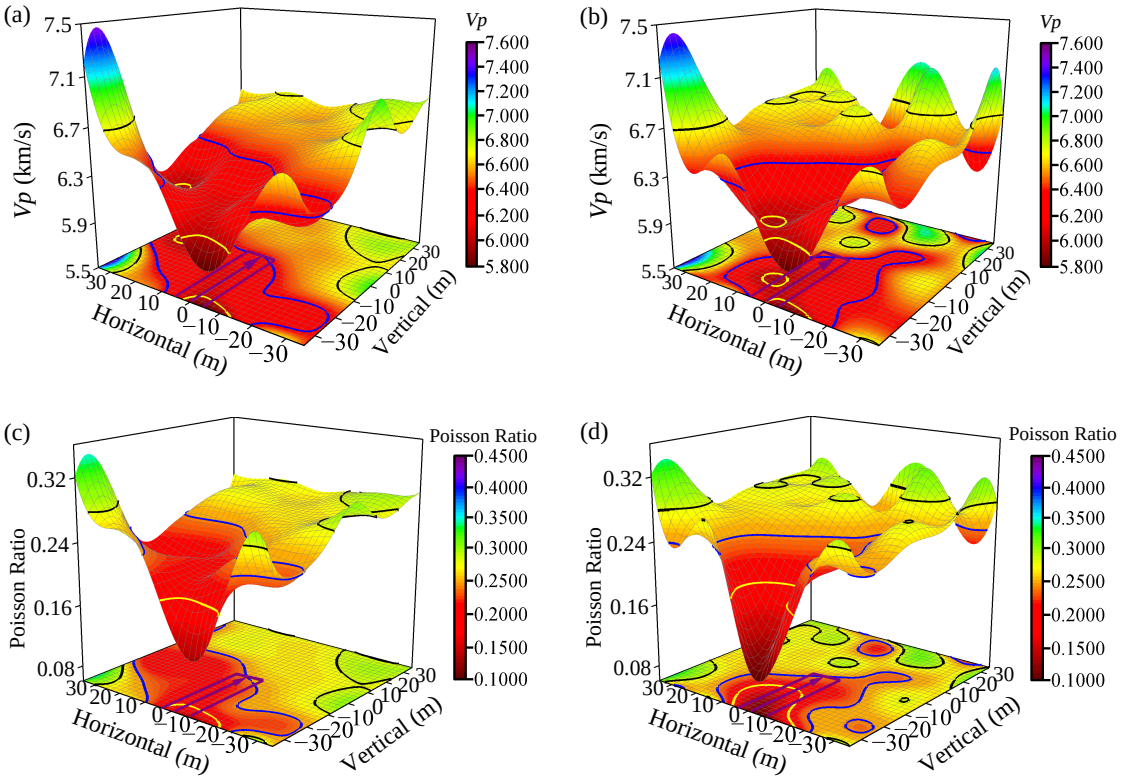


Fig. 10. Wave velocity and Poisson's ratio of the rock mass at the K42+685 monitoring section on 30th June: (a) 890-m floor (wave velocity), (b) 900-m roof (wave velocity), (c) 890-m floor (Poisson's ratio) and (d) 900-m roof (Poisson's ratio).

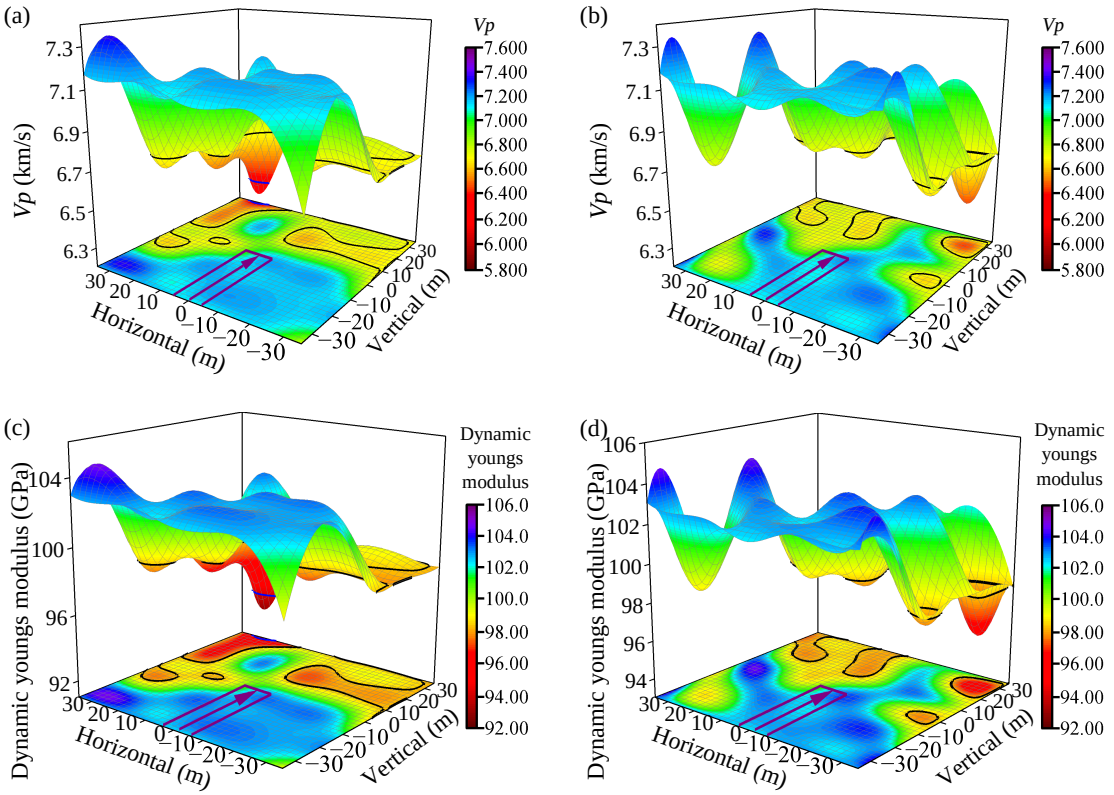


Fig. 11. Wave velocity and dynamic elastic modulus of the rock mass at the K42+685 monitoring section on 7th July: (a) 890-m floor (wave velocity), (b) 900-m roof (wave velocity), (c) 890-m floor (dynamic elastic modulus) and (d) 900-m roof (dynamic elastic modulus).

and the excavation of the tunnel face had a tremendous disturbance impact on the rock mass at the monitoring section, resulting in rock mass fragmentation and generally lower wave velocities.

Based on the established wave velocity-Poisson's ratio relationship, the corresponding Poisson's ratio distributions were further obtained to characterize the mechanical behavior of the surrounding rock. The calculated Poisson's ratio fields at the 890 m tunnel floor and 900 m tunnel roof are shown in Figs. 10(c) and 10(d). Both distributions exhibit low-value areas on the left side and middle regions, together with several high-value areas in the upper-left corner. Additionally, the 900-m roof has a few values higher than those of the 890-m floor. By 30th June, when the tunnel face had advanced approximately 3 m beyond section K42+685, intensified excavation disturbance induced unloading effects and micro-fracture development in the surrounding rock. The resulting damage zones were characterized by co-located anomalies associated with low velocity and low Poisson's ratio, particularly along both sidewalls. Since Eq. (20) enables the calculation of Poisson's ratio based on the wave velocity field, its spatial variation exhibits a distribution pattern consistent with the low-velocity zones.

4.2.3 Dynamic elastic modulus and V_p

To further characterize the recovery of and variation in the mechanical properties exhibited by the surrounding rock after excavation disturbance, the established relationship between V_p and mechanical parameters was utilized to obtain the dynamic elastic modulus. The dynamic elastic modulus was calculated according to Eq. (18). The spatial distributions of wave velocity and dynamic elastic modulus within a 30 m range of the K42+685 monitoring section on 7th July were comparatively analyzed, and the results are presented in Fig. 11. The V_p distributions are shown in Figs. 11(a) and 11(b). The rock mass V_p mostly exceeds 6.7 km/s, with the maximum value exceeding 7.3 km/s and the average wave velocity reaching 6.903 km/s. Specifically, the wave velocity is lower on the left side of the tunnel than that on the right side, and that in front of the monitoring section is lower than that that behind it, while the overall wave velocity remains relatively high. The reason for this relatively high average wave velocity is that by 7th July, the tunnel face had advanced to 38 m past the monitoring section. The rock mass at the observation cross-section experienced negligible excavation-induced disruption, owing to its considerable spatial separation from the advancing front. Moreover, the synergistic reinforcement provided by both the initial support and the secondary lining effectively consolidated the adjacent rock strata, and the micropores inside the rock were compacted, making the elastic wave propagation medium more continuous and resulting in higher rock mass wave velocities. In front of the monitoring section, low-velocity zones formed on both sides above the 890-m floor

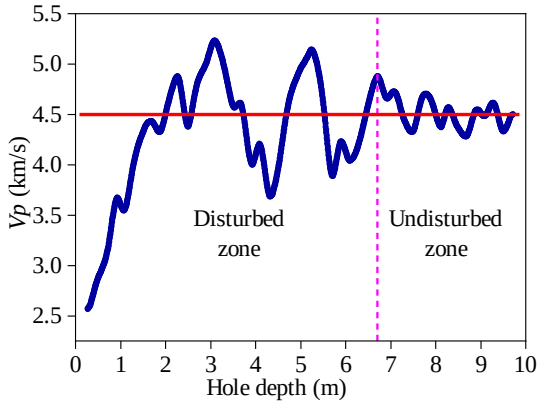


Fig. 12. Relationship between wave velocity and hole depth.

and below the 900-m roof, exhibiting asymmetry. This is because the asymmetric radial unloading of the rock mass induced the propagation of micro-fractures and stress relaxation. The deterioration of the continuity of the rock mass medium led the attenuation characteristics of the V_p values.

Based on the calculated V_p field, the dynamic elastic modulus distribution was further obtained to evaluate the mechanical response of the surrounding rock mass. The spatial distributions of dynamic elastic modulus at the 890 m tunnel floor and 900 m tunnel roof are shown in Figs. 11(c) and 11(d). Within the 30 m range of the tunnel, the left-side rock mass exhibits a lower dynamic elastic modulus relative to its right-side counterpart. Low dynamic elastic modulus areas exist in the upper-right corner of the 890-m floor and the lower-right corner of the 900-m roof. A comparison between Figs. 11(a) and 11(c), as well as between Figs. 11(b) and 11(d), demonstrates that the trends of variation in the calculated rock mass dynamic elastic modulus are roughly identical to those of the rock mass V_p during the same time period. On 7th July, both the wave velocity and dynamic elastic modulus of the rock mass at the K42+685 monitoring section were relatively high, indicating good rock mass quality. The dynamic elastic modulus of the rock mass calculated using Eq. (18) exhibits a similar spatial and temporal evolution pattern to that of the rock mass wave velocity. This is attributed to the direct relationship between the dynamic elastic modulus and V_p, indicating that the evolution of dynamic elastic modulus can effectively characterize the recovery of rock mass stiffness after excavation-induced degradation.

4.2.4 Compressive strength and V_p

Generally, Eq. (12) provides a relationship for determining the uniaxial compressive strength of the rock mass, which requires calculating the disturbance factor D. Under normal circumstances, $D > 0$, meaning that $V_{p,d} - V_{p,ud} < 0$. However, in a practical case study by Shen et al. (2010), where the wave velocity testing method was used to obtain rock mass wave velocities in order to calculate the rock mass wave velocity drop, the given relationship diagram between the wave velocity and hole depth (see Fig. 12) showed instances where $V_{p,d} - V_{p,ud} > 0$, i.e., $D < 0$. In this case, the calculated result of D is inconsistent with reality, which may be caused by the transfer and concentration of stress. To avoid computational instabilities from non-physical negative disturbance factors ($D < 0$), the quasi-rock mass compressive strength (R_{mc}) was adopted instead of the Hoek-Brown uniaxial strength (σ_{cm}). Unlike σ_{cm} based on empirical reduction, R_{mc} is rooted in elastic wave dynamics, directly linking V_p variations to rock damage evolution via the integrity index K_v.

The compressive strength of the quasi-rock mass is:

$$R_{mc} = \left(\frac{V_{pm}}{V_{pr}}\right)^2 R_c \tag{21}$$

where V_{pm} represents the P-wave velocity measured in the rock mass, V_{pr} denotes the measured P-wave velocity of intact rock determined through laboratory experiments, and R_c indicates the compressive strength obtained through laboratory testing of intact rock specimens. The rock mass integrity index is determined by squaring the ratio of the P-wave velocity in the rock mass to that of the intact rock, i.e., the rock mass integrity index $K_v = (V_{pm}/V_{pr})^2$, which indicates the degree of integrity exhibited by the rock mass.

The rock mass compressive strength was calculated using Eq. (21). The values of the parameters V_{pr} and R_c in the formula are closely related to the physico-mechanical properties of the rock block. Based on geological profile data for moderately weathered limestone in the experimental tunnel section, $R_c = 45$ MPa (rounded from 43.95 MPa) was selected as the reference parameter for the undamaged intact rock. To satisfy the physical relationship that the intact rock wave velocity must exceed both the *in-situ* jointed rock mass velocity and the initial V_p model ($V_{pm} = 6.7$ km/s), $V_{pr} = 7.5$ km/s was adopted to represent the wave velocity characteristics of intact rock free from excavation disturbances and structural defects. Here, V_{pr} serves purely as a reference parameter for calculating the quasi-rock mass compressive strength (R_{mc}) (Eq. (21)), rather than a velocity model constraint parameter in microseismic inversion. To evaluate parameter sensitivity under local lithological variations, the fluctuations of R_c and V_{pr} within ranges of $\pm 10\%$ and $\pm 15\%$ were analyzed. The results show that when R_c fluctuates, the range of R_{mc} values is between 32.33 and 41.31 MPa, and the magnitude of this variation is linearly related to R_c; when V_{pr} fluctuates, the range of R_{mc} values is between 27.15 and 45.00 MPa, with a variation amplitude of -24.4% to +25.3%, which is twice that of R_c but remains stably confined within the range of 27.15-45.00 MPa. Although these fluctuations affect the absolute value of R_{mc}, they do not alter the overall spatial trend of damage evolution in the surrounding rock.

After calculation, the wave velocity and compressive strength mappings of the rock mass within a 30 m range of the K42+685 monitoring section on 11th July are shown in Fig. 13. In Figs. 13(a) and 13(b), the rock mass wave velocity is basically maintained above 6.7 km/s, with low wave velocities in a few areas. The average wave velocity reaches 6.872 km/s, which is lower than the average rock mass wave velocity on 7th July (6.903 km/s), but the overall rock mass wave velocity is relatively high. Specifically, within the 30 m range of the tunnel, the left-side rock mass exhibits a lower wave velocity compared with the right-side rock mass, while that in front of the monitoring section is lower than

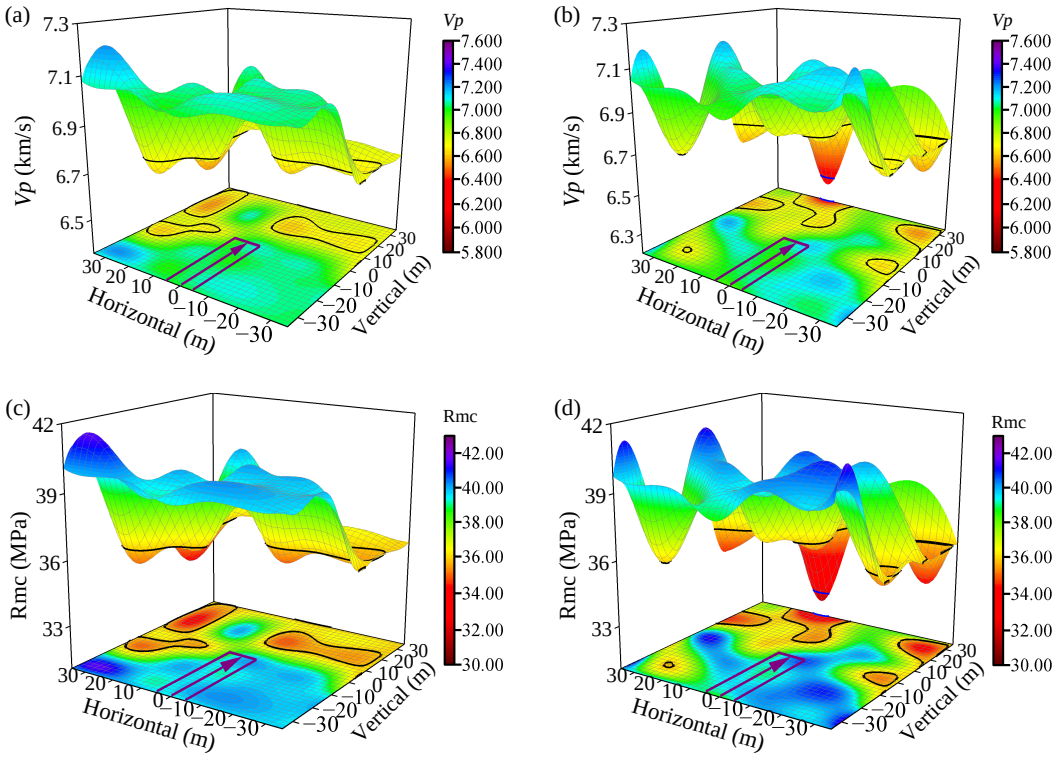


Fig. 13. Wave velocity and quasi-rock mass compressive strength at the K42+685 monitoring section on 11th July: (a) 890-m floor (wave velocity), (b) 900-m roof (wave velocity), (c) 890-m floor (compressive strength) and (d) 900-m roof (compressive strength).

that behind it. Low-velocity zones at the 890-m floor and 900-m roof are mainly distributed on both sides ahead of the monitoring section. At the floor, the low-velocity zone is relatively concentrated, whereas the corresponding area at the roof is more scattered. The reason is that by 11th July, the tunnel face had advanced to 46 m past the monitoring section. Due to the long distance, the excavation induced only limited alteration within the surrounding medium near the monitored cross-section. Moreover, constrained by the combined installation of the initial support system and the permanent lining, stress transfer or stress redistribution occurred within the rock mass, causing the average V_p of rock mass at this time to be lower than that on 7th July.

Based on the established wave velocity-compressive strength relationship, the corresponding compressive strength distribution was further obtained to characterize the mechanical state of the surrounding rock. The compressive strength distributions at the 890 m tunnel floor and 900 m tunnel roof are presented in Figs. 13(c) and 13(d), respectively. The calculated rock mass compressive strength using Eq. (21) shows variation trends consistent with those of the V_p. In areas where the wave velocity exceeds 6.7 km/s, i.e., where the compressive strength is greater than 35.912 MPa, the surrounding rock mass strength is relatively high. This manifests as the rock mass compressive strength on the left side being lower than the corresponding value for the right side within the 30 m range of the tunnel, with the compressive strength in front of the monitoring section being lower than that behind it. For 11th July, both the V_p and compressive strength of the rock mass at the K42+685 monitoring section are relatively high, indicating good rock mass quality. The variations in the rock mass compressive strength calculated using Eq. (21) are roughly identical to those of the rock mass wave velocity. Therefore, changes in the rock mass wave velocity can trigger corresponding changes in its compressive strength.

In summary, the time-varying wave velocity field obtained from microseismic TomoDD enables accurate 3D dynamic inversion of the physico-mechanical properties of tunnel surrounding rock. Their spatiotemporal evolution is highly consistent with V_p, revealing the spatial distribution, damage evolution, and degradation of the surrounding rock under excavation disturbance. This V_p-mechanical parameter conversion is mainly applicable to intact-to-moderately jointed rock masses dominated by excavation unloading; high porosity, severe weathering, strong anisotropy, high stress, or complex groundwater conditions may introduce uncertainties through nonlinear cracking and wave dispersion, requiring site-specific recalibration.

5. Dynamic analysis of rock mass BQ index

The BQ index is widely used in engineering rock mass classification and robustness evaluation. However, traditional methods based on geological surveys, laboratory tests, and st-

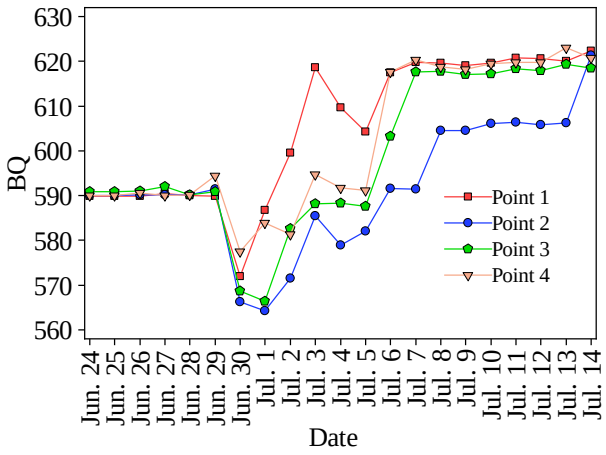


Fig. 14. Dynamic variations in BQ values at different monitoring points on the K42+685 section from 24th June to 14th July.

atic testing make it difficult to capture the dynamic evolution of surrounding rock during construction disturbances. Given the empirical correlations between wave velocity and rock mass properties, this study uses microseismic V_p as a proxy to dynamically estimate the BQ index and reflect changes in surrounding rock mass quality.

5.1 Relationship between BQ and V_p

In accordance with the Standard for Engineering Classification of Rock Mass (2015), the rock mass BQ index can be determined from the following equation:

$$\mathrm{BQ} = 100 + 3R_c + 250K_v \tag{22}$$

The calculation shall comply with the following provisions:

when $R_c > 90K_v + 30$, it shall be calculated as $R_c = 90K_v + 30$; i.e., $\mathrm{BQ} = 520K_v + 190$;

when $K_v > 0.04R_c + 0.4$, it shall be calculated as $K_v = 0.04R_c + 0.4$; i.e., $\mathrm{BQ} = 325K_v + 70$.

where $K_v = (V_{pm}/V_{pr})^2$.

Eq. (22) indicates that BQ has an obvious correlation with V_p, presenting a linear function relationship with K_v and a quadratic function relationship with the ratio of the rock mass elastic P-wave velocity to the intact rock elastic P-wave velocity.

However, when calculating BQ using Eq. (22), it is accompanied by strict piecewise constraints and exhibits poor continuity. Directly applying it to the dynamic inversion of BQ is highly prone to causing unrealistic jumps and abrupt mutations in the BQ values at critical threshold points. To overcome this discontinuity issue, building upon existing research, this study further derives and establishes a continuous linear relationship model between BQ and V_p.

Zhang et al. (2019) found that the BQ and RMR_{89} methods exhibit a certain correlation. Wu et al. (2023) conducted an in-depth analysis of multi-set rock mass classification data from multiple projects, discovered a highly linear correlation between BQ and RMR_{89}, and proposed the following equation:

$$\mathrm{BQ} = 5.6755\,\mathrm{RMR}_{89} + 130 \tag{23}$$

Combining the relationship linking GSI with the rock mass classification system RMR_{89} (Sabri et al., 2025) yields:

$$\mathrm{RMR}_{89} = 0.689\,\mathrm{GSI} + 13.518 \tag{24}$$

Then, substituting Eq. (10) yields the relationship equation between BQ and the P-wave velocity:

$$\mathrm{BQ} = 58.65629V_p + 196.94536 \tag{25}$$

Eq. (25) indicates a significant, continuous linear relationship between V_p and BQ. This derivation process, via introducing the RMR_{89} classification system and the GSI, effectively avoids the computational mutation risks of Eq. (22) and successfully merges the Chinese BQ standard with international rock mass evaluation systems. This establishes a more robust and universally applicable calculation formula for wave velocity and BQ. Furthermore, because the dynamic BQ index is directly derived from the inverted P-wave velocity field, its evaluation results are independent of the intact rock parameters (R_c and V_{pr}), making BQ classification immune to local lithological baseline fluctuations.

5.2 3D mapping and evolution of BQ index

By combining the time-varying V_p field of the surrounding rock mass inverted from microseismic monitoring, the relationship model between BQ and wave velocity can be utilized to dynamically estimate the BQ indices of the surrounding rock mass at the K42+685 section during different time periods. The trend of variation in rock mass quality classification index from 24th June to 14th July is thus obtained, as shown in Fig. 14.

To further evaluate the applicability of the wave velocity-BQ relationship model in characterizing variations in the surrounding rock quality during excavation, the temporal variations in the BQ values were analyzed and compared with the corresponding wave velocity changes. The calculated BQ index from 24th June to 14th July were found to exhibit trends consistent with the wave velocity variations at the four analysis points shown in Fig. 4(b). It can be observed that the variations in rock mass wave velocity effectively reflect the evolution of BQ index. This accurately captures the dynamic change process of surrounding rock quality during excavation unloading and support, in which the surrounding rock quality undergoes initial degradation followed by a stable recovery.

The BQ values of the rock mass were calculated using Eq. (25). The mappings of the rock mass wave velocity and its BQ within a 30 m range of the K42+685 monitoring section on 14th July are shown in Fig. 15. In Figs. 15(a) and 15(b), the rock mass wave velocity is basically maintained above 6.7 km/s, with an average wave velocity of 6.889 km/s. Falling between the average wave velocities on 7th July and 11th July, the overall rock mass wave velocity is relatively high. Specifically, the wave velocities in the middle and bottom-left areas of the rock mass are relatively high, while those in the bottom-right and top-right areas are relatively low. A small high-velocity zone can be seen in the top-left corner of the 890-m floor, whereas a small low-velocity zone exists in the top-left corner of the 900-hm roof. The reason is that by 14th

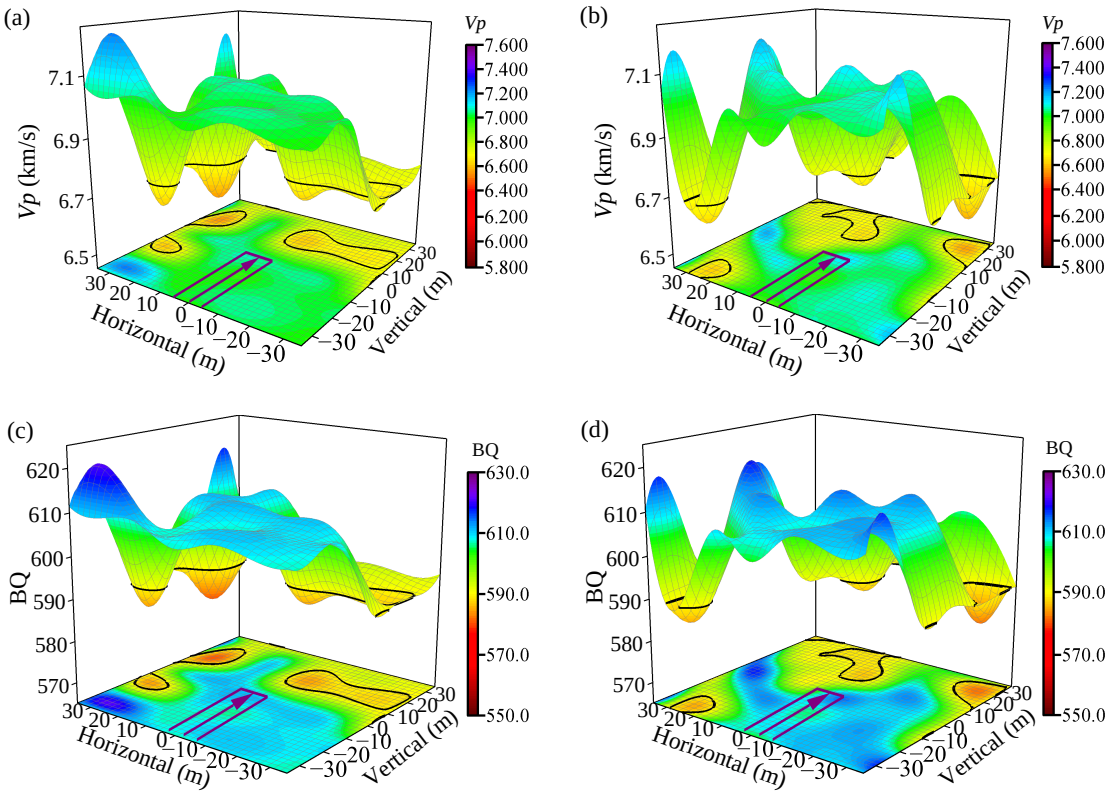


Fig. 15. Wave velocity and BQ mappings of the rock mass at the K42+685 monitoring section on 14th July: (a) 890-m floor (wave velocity); (b) 900-m roof (wave velocity); (c) 890-m floor (BQ); and (d) 900-m roof (BQ).

July, the tunnel face had advanced to 54 m past the monitoring section. Due to the long distance, the excavation had a very minor disturbance impact on the rock mass at the monitoring section. Furthermore, under the effects of previous primary support, secondary lining, and the transfer or redistribution of stress, the rock mass had stabilized, leading to relatively stable variations in the rock mass wave velocity.

To verify the spatial consistency between the wave velocity and the rock mass quality, the BQ distributions were further examined. As demonstrated by comparing Fig. 15(a) with 15(c) and Fig. 15(b) with 15(d), the areas with lower BQ values roughly correspond to the low wave velocity zones, and their variation trends are also largely identical. For 14th July, both the wave velocity and BQ values at the K42+685 monitoring section within the rock mass are relatively high, indicating good rock mass quality. The spatial distribution and variation trends of the rock mass BQ values calculated using Eq. (25) are consistent with those of the rock mass wave velocity. Therefore, the evolution of the BQ index provides a direct indication of the dynamic changes in rock mass quality during the excavation and support processes.

Comparative analysis of BQ distributions at different times identifies rock mass quality degradation zones and their evolution during construction. The time-varying BQ field inverted from microseismic wave velocity reflects spatial variations in rock mass quality and provides a reference for identifying potentially unstable zones.

6. Conclusions

Taking the theory of microseismic TomoDD as a basis, this study analyzed the dynamic evolution of the surrounding rock during tunnel construction. The main conclusions are as follows:

1) During the advancement of the tunnel face, the wave velocity of the surrounding rock exhibits extremely strong spatiotemporal evolution laws. Due to differences in the surrounding rock properties or support structures, the variations in wave velocity show obvious asymmetry. At different times, the magnitudes of wave velocity of the surrounding rock are clearly different, presenting dynamic variation characteristics, which accurately maps the entire process of dynamic stress redistribution in the tunnel surrounding rock.
2) By comparing the wave velocity evolution images of the tunnel floor (890 m) and roof (900 m), the formation, expansion and migration paths of low-velocity zones under excavation disturbance were clearly identified, achieving 3D visual tracking of hidden hazards in the excavation disturbed zone.
3) Based on the inverted wave velocity data and the dynamic conversion model between the wave velocity and the mechanical parameters, accurate and efficient 3D dynamic estimations of the mechanical parameters of the tunnel surrounding rock could be performed, intuitively reflect-

ing the structural degradation caused by microfracture development.

4) According to the microseismic time-lapse wave velocity field, the dynamic spatial distribution of the BQ values of the surrounding rock is inverted, clearly identifying the spatiotemporal variation trends of the BQ index of the surrounding rock and realizing the real-time and efficient determination of the surrounding rock classification. This effectively overcomes the spatiotemporal limitations of traditional point-based investigations.

Acknowledgements

The authors would like to gratefully acknowledge the financial assistance provided by the National Key Research and Development Program Young Scientists Project (No. 2022YFC2905700), the National Natural Science Foundation of China (No. 52274176), the Key Project for Technological Innovation and Application Development in Chongqing (Nos. CSTB2024TIAD-KPX0102 and CSTB2025TIAD-KPX0029), and the Research and Innovation Program for Graduate Students in Chongqing (No. CYS260520).

Conflicts of interest

The authors declare no competing interest.

Open Access This article is distributed under the terms and conditions of the Creative Commons Attribution (CC BY-NC-ND) license, which permits unrestricted use, distribution, and reproduction in any medium, provided the original work is properly cited.

References

Ben Ghawar, B. M., Zairi, M., Bouaziz, S. Verification of Gardner's equation and derivation of an empirical equation for anhydrite rocks in Sirte basin, Libya: Case study. Heliyon, 2021, 7(1): e06017.

Chen, Y., Zhang, H., Miao, Y., et al. Back-azimuth constrained double-difference seismic location and tomography for downhole microseismic monitoring. Physics of the Earth and Planetary Interiors, 2017, 264: 35-46.

Cui, L., Zheng, J., Dong, Y., et al. Prediction of critical strains and critical support pressures for circular tunnel excavated in strain-softening rock mass. Engineering Geology, 2017, 224: 43-61.

Deng, S., Zhang, W., Yu, X., et al. Analysis on crustal structure characteristics of southern Sichuan-Yunnan by regional double-difference seismic tomography. Chinese Journal of Geophysics, 2020, 63(10): 3653-3668. (in Chinese)

Feng, W., Dong, S., Wang, Q., et al. Improving the Hoek-Brown criterion based on the disturbance factor and geological strength index quantification. International Journal of Rock Mechanics and Mining Sciences, 2018, 108: 96-104.

Gardner, G. H. F., Gardner, L. W., Gregory, A. R. Formation velocity and density: The diagnostic basics for stratigraphic traps. Geophysics, 1974, 39(6): 770-780.

GB/T 50218-2014. Standard for Engineering Classification of Rock Mass. Beijing: China Planning Press, 2015. (in Chinese)

Guo, H., Sun, Q., Feng, G., et al. In-situ observations of damage-fracture evolution in surrounding rock upon unloading in 2400-m-deep tunnels. International Journal of Mining Science and Technology, 2023, 33(4): 437-446.

Guo, S., Zhang, Y., Iraji, A., et al. Assessment of rock geomechanical properties and estimation of wave velocities. Acta Geophysica, 2023, 71: 649-670.

Hoek, E., Brown, E. T. Practical estimates of rock mass strength. International Journal of Rock Mechanics and Mining Sciences, 1997, 34(8): 1165-1186.

Hoek, E., Brown, E. T. The Hoek-Brown failure criterion and GSI - 2018 edition. Journal of Rock Mechanics and Geotechnical Engineering, 2019, 11(3): 445-463.

Hoek, E., Carranza-Torres, C., Corkum, B. Hoek-Brown failure criterion - 2002 edition. Paper Presented at NARMS-TAC 2002: the 5th North American Rock Mechanics Symposium and the 17th Tunnelling Association of Canada Conference, Toronto, Ontario, 7-10 July, 2002.

Huang, S., Li, X., Zhao, T., et al. Effect of support friction on mixed mode I-II fracture behavior of compacted clay: Numerical and experimental study. Engineering Fracture Mechanics, 2026, 335: 111917.

Kong, L., Yan, P., Liu, X., et al. Estimating the mechanical and dynamic parameters in surrounding rock mass of tunnels based on velocities of blasting seismic waves. Tunnelling and Underground Space Technology, 2025, 165: 106897.

Li, H., Qu, X., Lin, J., et al. Formation mechanisms of high-quality ultra-deep clastic reservoirs: Progress, scientific challenges and future directions. Advances in Geo-Energy Research, 2026, 21(3): 201-204.

Li, X., Zhang, X., Liu, Q., et al. Evaluation of rock mass quality and its mechanical properties through digital drilling process monitoring. Journal of Rock Mechanics and Geotechnical Engineering, 2025, 17(7): 4490-4511.

Li, Z., Yang, Z., Fu, M., et al. A geometric variation method to extract rock strength parameters via uniaxial compression testing. International Journal of Rock Mechanics and Mining Sciences, 2024, 178: 105755.

Ma, T. H., Tang, C. A., Tang, S. B., et al. Rockburst mechanism and prediction based on microseismic monitoring. International Journal of Rock Mechanics and Mining Sciences, 2018, 110: 177-188.

Marinos, P., Hoek, E. Estimating the geotechnical properties of heterogeneous rock masses such as flysch. Bulletin of Engineering Geology and the Environment, 2001, 60(2): 85-92.

Qian, J., Zhang, H., Westman, E. New time-lapse seismic tomographic scheme based on double-difference tomography and its application in monitoring temporal velocity variations caused by underground coal mining. Geophysical Journal International, 2018, 215(3): 2093-2104.

Rahman, T., Sarkar, K. Correlations between uniaxial compressive strength and dynamic elastic properties for six rock types. International Journal of Geomechanics, 2023, 23(6): 04023064.

Rahman, T., Sarkar, K., Singh, A. K. Correlation of geomechanical and dynamic elastic properties with the P-wave

velocity of Lower Gondwana coal measure rocks of India. International Journal of Geomechanics, 2020, 20(10): 04020189.

Sabri, M. S., Jaiswal, A., Verma, A. K., et al. Systematic review of RMR, Q-system, and GSI in tunnel classification: Origin, advancement, and limitations. Indian Geotechnical Journal, 2025, https://doi.org/10.1007/s40098-025-01401-5. (in Press)

Shen, Y., Xu, G., Zhang, L., et al. Research on characteristics of rock deformation caused by excavation disturbance based on Hoek-Brown criterion. Chinese Journal of Rock Mechanics and Engineering, 2010, 29(7): 1355-1362. (in Chinese)

Somodi, G., Krupa, Á., Kovács, L., et al. Comparison of different calculation methods of geological strength index (GSI) in a specific underground construction site. Engineering Geology, 2018, 243: 50-58.

Sun, Y., Xu, N., Xiao, P., et al. Characterizing large deformation of soft rock tunnel using microseismic monitoring and numerical simulation. Journal of Rock Mechanics and Geotechnical Engineering, 2025, 17(1): 309-322.

Sun, Z., Zhang, D., Hou, Y., et al. Support countermeasures for large deformation in a deep tunnel in layered shale with high geostresses. Rock Mechanics and Rock Engineering, 2023, 56(6): 4463-4484.

Waldhauser, F., Ellsworth, W. L. A double-difference earthquake location algorithm: Method and application to the northern Hayward fault, California. Bulletin of the Seismological Society of America, 2000, 90(6): 1353-1368.

Wu, A., Zhao, W., Zhang, Y., et al. A detailed study of the CHN-BQ rock mass classification method and its correlations with RMR and Q system and Hoek-Brown criterion. International Journal of Rock Mechanics and Mining Sciences, 2023, 162: 105290.

Wu, A., Liu, F. Advancement and application of the standard of engineering classification of rock masses. Chinese Journal of Rock Mechanics and Engineering, 2012, 31(8): 1513-1523. (in Chinese)

Wu, L., Adoko, A. C., Li, B. An illustration of determining quantitatively the rock mass quality parameters of the Hoek-Brown failure criterion. Rock Mechanics and Rock Engineering, 2018, 51(4): 1063-1076.

Xia, K., Chen, C., Liu, X., et al. Estimating shear strength of high-level pillars supported with cemented backfilling using the Hoek-Brown strength criterion. Journal of Rock Mechanics and Geotechnical Engineering, 2024, 16(2): 454-469.

Xia, K., Chen, C., Wang, T., et al. Quantification of the GSI and D values in the Hoek-Brown criterion using the rock quality designation (RQD) and discontinuity surface condition rating (SCR). Bulletin of Engineering Geology and the Environment, 2022, 81(1): 4.

Xia, K., Chen, C., Wang, T., et al. Estimating the geological strength index and disturbance factor in the Hoek-Brown criterion using the acoustic wave velocity in the rock mass. Engineering Geology, 2022, 306: 106745.

Yang, H., Jiang, C., Li, Y., et al. Experimental study on real-time monitoring of surrounding rock 3D wave velocity structure and failure zone in deep tunnels. International Journal of Mining Science and Technology, 2026, 36(2): 423-437.

Yang, H., Zhang, Z., Wang, X., et al. The study on the application of time-lapse double-difference tomography theory in the 3D velocity structure distribution of tunnel surrounding rock. Rock Mechanics and Rock Engineering, 2026, online.

Zhan, Q., Tang, L., Wang, Y., et al. Study on the stress and deformation characteristics of ultra-deep soft rock tunnel under complex geological conditions. Scientific Reports, 2024, 14(1): 28894.

Zhang, H., Thurber, C. H. Double-difference tomography: The method and its application to the Hayward Fault, California. Bulletin of the Seismological Society of America, 2003, 93(5): 1875-1889.

Zhang, H., Thurber, C. H. Development and applications of double-difference seismic tomography. Pure and Applied Geophysics, 2006, 163(2-3): 373-403.

Zhang, Q., Huang, X., Zhu, H., et al. Quantitative assessments of the correlations between rock mass rating (RMR) and geological strength index (GSI). Tunnelling and Underground Space Technology, 2019, 83: 73-81.

Zhang, S., Li, C., Ran, C., et al. Unified model for shear strength of soft and hard rock masses based on *in-situ* direct shear test parameters. International Journal of Non-Linear Mechanics, 2026, 180: 105233.

Zhao, Y., Yang, T., Zhang, P., et al. The analysis of rock damage process based on the microseismic monitoring and numerical simulations. Tunnelling and Underground Space Technology, 2017, 69: 1-17.